nature physics

Article

https://doi.org/10.1038/s41567-026-03383-4

Time-resolved imaging of antiferromagnetic skyrmion interactions

Received: 26 August 2025

Accepted: 24 June 2026

Published online: 10 August 2026

Check for updates

Mona Bhukta[1,12], Takaaki Dohi[1,2,12] ✉, Kilian Leutner[1,12], Maria-Andromachi Syskaki[1,3], Fabian Kammerbauer[1], Duc Minh Tran[1], Sebastian Wintz[4,5], Markus Weigand[4], Simone Finizio[6], Jörg Raabe[6], Hendrik Ohldag[7,8,9], Thibaud Denneulin[10], Joseph Vimal Vas[10], Rafal E. Dunin-Borkowski[10], Robert Frömter[1] ✉ & Mathias Kläui[1,11] ✉

Quantifying particle interactions is central to understanding and controlling collective dynamics in particle-based devices such as those comprising skyrmion ensembles. Here we directly visualize, in real time, the nanosecond current-driven dynamics of an antiferromagnetic skyrmion lattice. By tuning the spin–orbit torque relative to local pinning, we identify two regimes: an incoherent flow, where mobile skyrmions are driven toward pinned neighbours undergoing compression followed by a recoil, and a coherent flow regime, where the lattice translates uniformly. We use an inverse analysis method based on the Thiele equation to extract an exponentially decaying antiferromagnetic skyrmion interaction potential, which is in agreement with simulation results. At higher current densities, the lattice exhibits coherent motion free from detectable Hall and inertial effects or dynamical deformation, and this enables robust ultrafast operation. These findings establish a quantitative framework for antiferromagnetic skyrmion interactions and demonstrate deterministic control of their collective dynamics, even in the incoherent flow regime, thereby providing potential applications for multiskyrmion spintronic devices.

In the pursuit of post-complementary metal-oxide semiconductor technologies, spintronic devices have garnered growing interest for their non-volatility, energy efficiency and scalability[1,2]. Among various information carriers that are being proposed, skyrmions, which are topologically non-trivial spin textures[3–6], have emerged as strong candidates, owing to their size down to the nanometre regime, topologically enhanced stability[7,8] and susceptibility to manipulation by electrical currents[9–11]. Although skyrmions in ferromagnets enabled seminal advances in racetrack memories[5,12,13], logic gates[14] and unconventional computing concepts[15,16], their practical utility is hampered by stray fields, limited thermal stability and the intrinsic skyrmion Hall effect (SkHE)[10,11]. Within this context, antiferromagnetic (AFM) skyrmions have risen to prominence as compelling candidates. Their vanishing net topological charge suppresses the SkHE, enabling rectilinear motion under applied currents[17–19] and enhances their ultrafast response to external stimuli[20]. In synthetic AFMs (SyAFMs), where two ferromagnetic layers are coupled antiferromagnetically through an ultrathin non-magnetic spacer, angular-momentum compensation

[1]Institute of Physics, Johannes Gutenberg University Mainz, Mainz, Germany. [2]Laboratory for Nanoelectronics and Spintronics, Research Institute of Electrical Communication, Tohoku University, Sendai, Japan. [3]Singulus Technologies AG, Kahl am Main, Germany. [4]Helmholtz-Zentrum Berlin für Materialien und Energie GmbH, Berlin, Germany. [5]Max Planck Institute for Intelligent Systems, Stuttgart, Germany. [6]Swiss Light Source, Paul Scherrer Institut, Villigen, Switzerland. [7]Advanced Light Source, Lawrence Berkeley National Laboratory, Berkeley, CA, USA. [8]Department of Physics, University of California Santa Cruz, Santa Cruz, CA, USA. [9]Department of Materials Science and Engineering, Stanford University, Stanford, CA, USA. [10]Ernst Ruska-Centre for Microscopy and Spectroscopy with Electrons, Forschungszentrum Jülich, Jülich, Germany. [11]Center for Quantum Spintronics, Department of Physics, Norwegian University of Science and Technology, Trondheim, Norway. [12]These authors contributed equally: Mona Bhukta, Takaaki Dohi, Kilian Leutner. ✉e-mail: takaaki.dohi.e5@tohoku.ac.jp; froemter@uni-mainz.de; klaeui@uni-mainz.de

cancels the gyrotropic force, allowing spin–orbit torque (SOT)-driven velocities approaching 1 km s^{-1} (ref. 21). Furthermore, the suppression of stray fields facilitates miniaturization[22], offering decisive advantages for ultrahigh-density spintronic integration.

A key challenge for deterministic skyrmion-based spintronic devices[15,16] is achieving reproducible dynamics, which has so far only been demonstrated for single FM skyrmions without substantial interactions. However, as more complex multiskyrmion dynamics enable a wider range of applications[23], the deterministic dynamics also have to be realized in dense skyrmion lattice ensembles, where the minimum skyrmion spacing sets limits on both storage density and signal fidelity. In this regime, skyrmion–skyrmion interactions[24–28] and scattering become essential design parameters, as they drive transient deformation and relaxation that shape the collective dynamics. Quantitative knowledge of these inherent transient processes is therefore critical for device functionality, which remains inaccessible to conventional quasi-static imaging techniques. For example, device clock frequency, a key determinant of computational performance, is governed both by the steady-state skyrmion velocity and by transient inertial responses on nanosecond timescales. Although time-resolved microscopy has revealed a range of nanosecond-scale dynamical phenomena in FM skyrmions, such as nucleation[29], annihilation[30], current-induced motion[11] and chaotic responses[31], analogous behaviour remains elusive for AFM skyrmions. Although fractional AFM skyrmion lattices have been reported[32], their real-space dynamical investigation remains experimentally unexplored, despite their unique potential to combine suppression of the SkHE and direct probing of skyrmion–skyrmion interactions. Such a platform would provide access to transient non-equilibrium dynamics at nanometre-scale spacing, including repulsion, scattering, deformation and relaxation, while also enabling the study of emergent transport signatures such as the topological spin Hall effect[33] and the topological orbital Hall effect[34]. However, probing these processes is experimentally challenging, as conventionally used quasi-static imaging cannot capture processes that unfold on nanosecond timescales. So these challenges call for time-resolved microscopy measurements to reveal skyrmion scattering, skyrmion–skyrmion interactions, lattice stability and dynamical response in AFM systems.

Here, we employ pump–probe X-ray microscopy with high spatiotemporal resolution (20-nm spatial and 1-ns temporal) to resolve the real-space trajectories and dynamic behaviour of an interacting AFM skyrmion lattice in a SyAFM. Element-specific magnetic contrast allows for dynamic visualization of both sublattices, providing direct access to their coupled dynamics and enabling observation of skyrmion–skyrmion interactions as scattering, recoil and collective flow. When SOT is comparable to local pinning potentials, the system enters an incoherent regime in which mobile and pinned skyrmions coexist. Upon removal of the drive, mobile skyrmions recoil after scattering from pinned neighbours, exhibiting an exponential slowdown with characteristic timescales of 3–20 ns, thereby probing the local potential and quantifying the skyrmion–skyrmion repulsion's spatial range and timescale. By simultaneously applying an inverse estimation method based on the Thiele equation[21,35,36] to all measured relaxation trajectories, we quantitatively map the skyrmion interaction potential, continuously from a compressed state into a relaxed state, revealing an exponential decay as well as the fundamental length scale of the interaction. At higher currents, pinning is overcome and the lattice flows coherently in a nearly flat energy landscape. Angular-momentum compensation suppresses the SkHE, and time-resolved imaging reveals uniform translation without internal deformation, Hall deflection or inertial lag. This establishes the operational window for deterministic skyrmion transport and robust gigahertz-speed functionality. Together, these results provide a quantitative framework for AFM skyrmion interactions and demonstrate control of their collective dynamics, paving the way for scalable, high-speed spintronic devices.

Pump–probe X-ray microscopy on AFM skyrmion lattices

To investigate skyrmion–skyrmion interactions as well as the transient response of the AFM skyrmion lattice to the spin torque, we prepared and optimized a low-pinning SyAFM stack comprising thin multilayers with two alternating ferromagnetic sublattices (A and B), as illustrated in Fig. 1a (see the Methods for more details). The Pt and Ir interfaces break inversion symmetry, introducing a strong interfacial Dzyaloshinskii–Moriya interaction (DMI)[37,38] into the system. By precisely tuning the thickness and composition of the ferromagnetic sublattices, we stabilize AFM skyrmions at varying levels of magnetic compensation within the SyAFM, as demonstrated in prior studies[20,39,40]. In this work, the magnetic system was tuned to obtain full magnetization compensation, as evidenced by the hysteresis curves measured using a superconducting quantum interference device (SQUID) magnetometer, shown in Supplementary Section A1. The strategic incorporation of Fe-rich and Co-rich FM layers into the two FM sublattices enables independent probing of each sublattice via X-ray imaging, providing a direct method to visualize the AFM skyrmion lattice. The uniqueness of our experimental setup opens the door to sublattice-resolved studies of pinning potentials as well as transient response, a key determinant of spin-texture dynamics in any magnetic system with multiple sublattices. Scanning transmission X-ray microscopy (STXM) performed at the Fe L_3 (Fig. 1b) and Co L_3 (Fig. 1c) absorption edges reveals an inverted skyrmion contrast between sublattices A and B. This inversion reflects the antiparallel out-of-plane magnetization in adjacent layers, confirming robust AFM interlayer exchange coupling across the multilayer stack. Within this framework, skyrmions in sublattice A exhibit a topological charge of $Q_A = +1$, whereas those in sublattice B carry $Q_B = -1$. Together, they constitute an AFM skyrmion lattice, as depicted in Fig. 1d, obtained from micromagnetic simulations (Supplementary Section B2). To investigate the AFM skyrmion dynamics in these systems, the SyAFM multilayer films were patterned into 5 µm-wide, 2 µm-long magnetic strips as shown in Fig. 1e.

At room temperature and zero magnetic field, the as-grown state of the SyAFM exhibits a multidomain configuration with a labyrinth character. By applying a series of bipolar pulses[41] to this state, we nucleate an AFM skyrmion lattice. The magnetic field dependence of the AFM skyrmion lattice, as shown in Supplementary Fig. 2, reveals its stability over a wide range of out-of-plane fields from −250 mT to +250 mT. This robustness arises from its insensitivity to magnetic fields, which reflects its AFM nature. We apply alternating bipolar current pulses that drive the skyrmions back and forth by equal distances, ensuring the restoration of the initial state after each pump cycle. The 70–100-ps X-ray probe pulses from the storage ring are synchronized with the pump pulses at varying delays, enabling time-resolved imaging. Each frame in a so-obtained movie corresponds to a specific timepoint within the excitation sequence, capturing the transient magnetic states during motion. Since the magnetic contrast in the experiment is averaged over billions of bipolar excitation cycles, any non-reproducible skyrmion motion will average out and will not be visible. Reproducibility in the skyrmion lattice dynamics is therefore pivotal for pump–probe dynamic measurements, which rely on precise and distinguishable signals to analyse dynamic trajectories. Moreover, as the imaging method is based on photon transmission through the multilayer stack, the resulting magnetization contrast reflects an average over all repeated layers (Methods), suppressing contributions from rare, non-recurring events.

Real-time imaging of incoherent skyrmion lattice dynamics

In an AFM skyrmion lattice, long-range dipolar stray fields are suppressed, and short-range exchange and DMI, together with local anisotropy, dominate, setting the equilibrium lattice spacing. This is in stark contrast to ferromagnetic skyrmion lattices, where long-range

https://doi.org/10.1038/s41567-026-03383-4

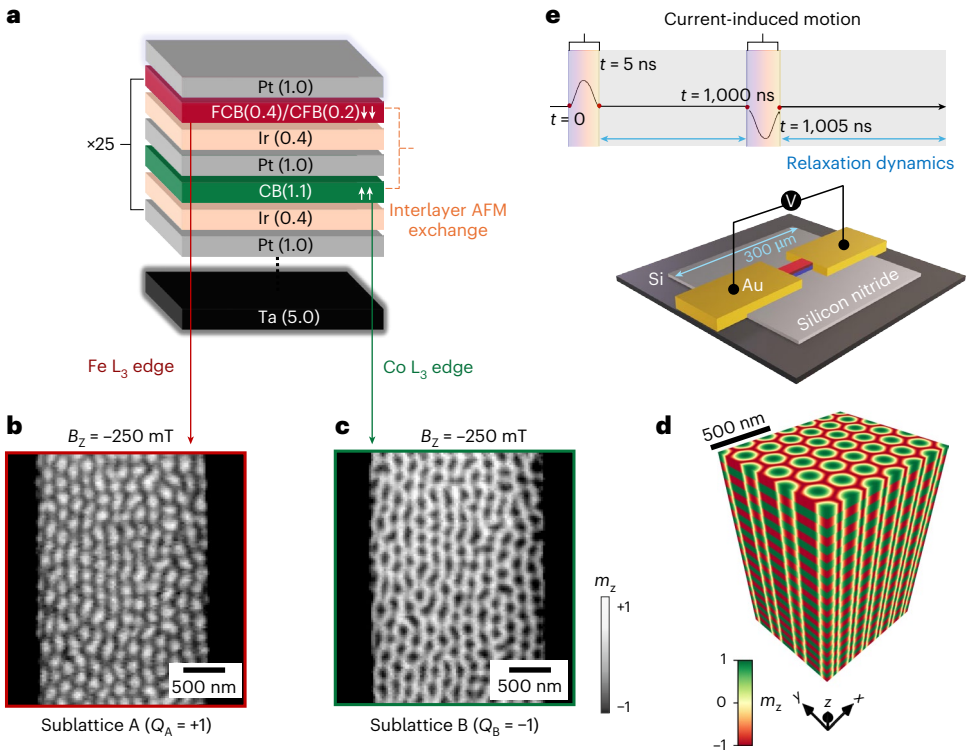


Fig. 1 | Static imaging of the AFM skyrmion lattice. a, A schematic of the SyAFM multilayer stack composed of Fe-rich (sublattice A, red) and Co-rich (sublattice B, green) ferromagnetic layers, antiferromagnetically coupled via Ir spacers. **b**,**c**, Sublattice-selective X-ray imaging of the AFM skyrmion lattice at the Fe (**b**) and Co (**c**) L_3 absorption edges. The inverted magnetic contrast between sublattices confirms robust AFM coupling of the skyrmion lattice throughout the multilayer. **d**, Three-dimensional micromagnetic simulation of the AFM skyrmion lattice in the SyAFM stack, showing alternating out-of-plane magnetization in adjacent layers (*z* axis not to scale). **e**, Device layout and schematic temporal pump-pulse pattern. The SyAFM is deposited on a SiN membrane window with gold contact pads for bipolar current pulse excitation. In **b**–**d**, the grey scale/colour scale denotes the normalized out-of-plane magnetization component (m_z), with ($m_z = +1$) and ($m_z = -1$) corresponding to opposite out-of-plane magnetization directions.

dipolar interactions dominate over other contributions[25,42]. When subjected to weak excitations, the AFM lattice is driven out of equilibrium: pinned skyrmions serve as scattering centres for mobile ones, leading to either local lattice compression or trajectory deflection. Such scattering events encode the skyrmion–skyrmion interaction potential, which can be quantitatively extracted from measured real-space trajectories. Fully compensated SyAFMs offer an ideal platform for this, as the cancellation of gyrotropic terms suppresses the skyrmion Hall effect[19,21], isolating longitudinal motion and potentially enabling a direct mapping between scattering geometry and interaction forces. To resolve the spatiotemporal dynamics of an AFM skyrmion lattice, we employ pump–probe X-ray microscopy, which enables real-time nanosecond tracking of individual skyrmion trajectories. This provides direct access to transient effects, such as skyrmion–skyrmion repulsion and inertial responses, that are not resolved in quasi-static measurements. To observe the dynamics of each magnetic sublattice, we perform sequential measurements at the Fe and Co L_3 absorption edges, as only one X-ray energy can be used at a time.

We first discuss the low-current regime ($J_x = 2.8 \times 10^{11}$ A m^{-2}), where the strength of the current-induced SOT is comparable to the local pinning potential. In this case, motion is governed by a spatially inhomogeneous energy landscape, where variations in pinning strength give rise to an incoherent dynamical regime in which different parts of the lattice respond differently to the same uniform drive. Despite the application of a uniform current, the lattice response is spatially heterogeneous: some skyrmions remain pinned (for example, I1 in Fig. 2a), others translate smoothly (for example, M1 in Fig. 2a), and some undergo pronounced deformation (for example, R1 in Fig. 2a). The pinning sites correspond to energy minima associated with material inhomogeneities, defects or grain boundaries that locally suppress skyrmion mobility. To address these strongly differing motion patterns within the imaged skyrmion ensemble, we conduct a classification of skyrmions into four clusters, as colour coded in Fig. 2a, according to their net displacement during current excitation: immobile skyrmions (class I, blue), mobile skyrmions (class M, red) and those located immediately adjacent to the mobile cluster on the left (class L, green) and right (class R, black). Class M skyrmions exhibit a large displacement during the pulse, whereas class I skyrmions show only minimal motion. We define this behaviour as an incoherent flow regime, where skyrmions in both sublattices move in synchrony, yet the overall lattice response remains spatially fragmented. The dynamics are highly reproducible across all cycles, confirming their non-stochastic origin. The effects of thermal fluctuations, which generate statistically random variations that average out in pump–probe measurements, are therefore not detectable in the present study; consequently, a thermally activated creep regime, while in principle potentially present in skyrmion lattice dynamics, is not resolved. The local behaviour varies substantially, from pinned to deforming skyrmions and to those undergoing smooth displacements. The spatial distribution of displacements (Fig. 2a) shows that this response extends throughout the interior rather than being localized at device edges, indicating that the energy landscape is governed by distributed microstructural disorder rather than geometric confinement. Such spatial heterogeneity under uniform excitation reflects a breakdown of global lattice coherence and distinguishes this particular regime from both thermally activated creep and viscous-flow regimes.

Figure 2b shows the evolution of skyrmion contours in sublattice A under a current pulse applied along the *x* axis, revealing their time-resolved response to SOTs during a pump cycle. The contours

https://doi.org/10.1038/s41567-026-03383-4

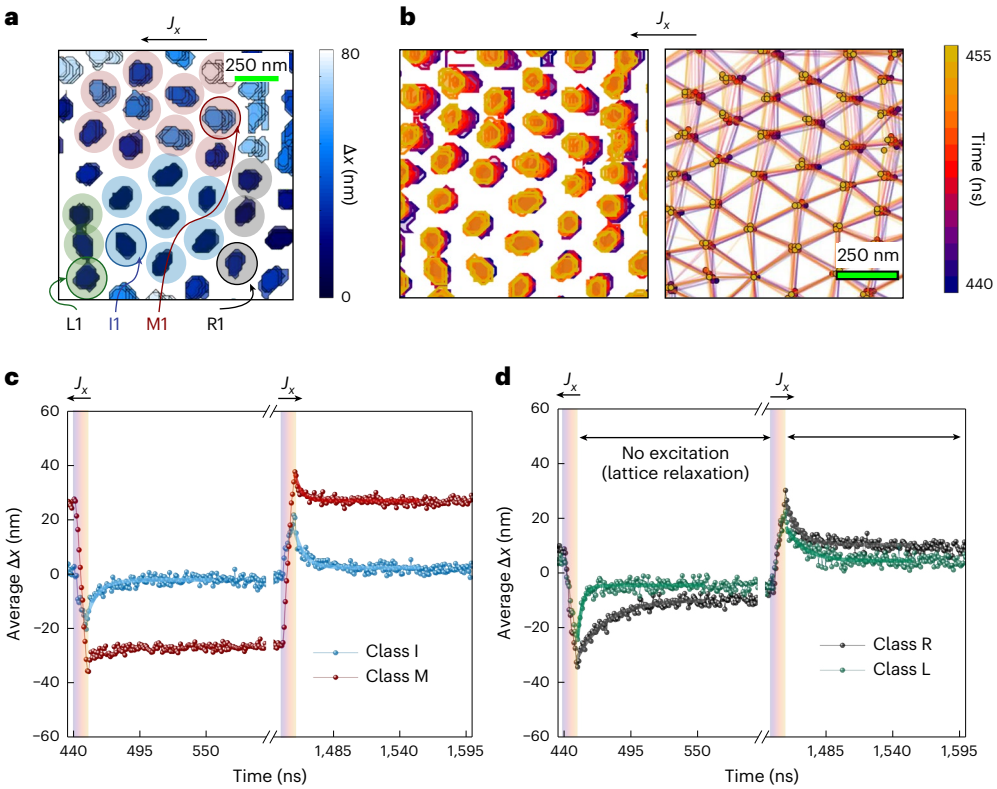


Fig. 2 | Spatio-temporal evolution of an AFM skyrmion lattice during the cycle of bipolar current pulses. a, x-displacement map following a negative pulse, used to classify the skyrmions into four categories: immobile (I, blue), mobile (M, red), laterally adjacent to the left (L, green) and to the right (R, black) of the mobile region. The colour scale encodes the net displacement along the x direction. Circles indicate representative skyrmions from each class exhibiting distinct responses to current excitation. **b**, Time-resolved evolution of AFM skyrmions under a current pulse ($J_x = -2.8 \times 10^{11}$ A m^{-2}). Left: skyrmion contours extracted from STXM images, colour-coded by time over the displayed 15-ns interval (purple to yellow). Right: corresponding particle representation, where skyrmion cores are modelled as point particles and Delaunay triangulations are constructed at each time step using the same time colour scale. **c**,**d**, Average displacement traces for class I and M (**c**) and L and R (**d**). Shaded regions indicate the duration of the negative and positive current pulses during the bipolar pulse. Upon pulse termination, all skyrmion classes exhibit recoil opposite to their preceding motion, regardless of previous current polarity. I and M skyrmion classes, with the I skyrmions showing the strongest recoil and M types the weakest, are shown. The L and R skyrmion classes display asymmetric recoil dynamics, governed by their lateral position relative to the immobile class I. All timescales for the recoil dynamics, as extracted via exponential fitting, fall within 3–20 ns.

in Fig. 2b, left, are colour-coded over a 15-ns window, from purple at early times to yellow at late times, visualizing the progression of skyrmion boundary displacement. These contours are obtained by tracking individual skyrmion boundaries across consecutive frames. To analyse local lattice deformation, the skyrmion cores are modelled as point particles and Delaunay triangulations are constructed at each time step, as shown in Fig. 2b, right. This representation depicts the evolving geometry and local strain within the lattice during current excitation. Both sublattices A and B exhibit synchronized skyrmion motion (Supplementary Fig. 3 for sublattice B), following identical trajectories. The synchronized motion of both sublattices, despite the spatially heterogeneous response, shows that even the relatively weak interlayer AFM exchange in thin-film SyAFMs, compared with the strong intrinsic exchange in bulk antiferromagnets, is sufficient to overcome local pinning, enabling robust sublattice locking and offering a key advantage for AFM spintronic applications.

Pinned skyrmions act as rigid obstacles within the lattice, inducing constraints that can be described in a mechanical approach and lead to anisotropic strain in neighbouring skyrmions. As adjacent skyrmions are pushed by the applied current, these constraints result in boundary elongation or compression. For instance, skyrmions located just outside the boundary of pinned regions (for example, R1) cannot translate freely; instead, one domain wall is effectively anchored by the adjacent pinned skyrmion, while the opposite boundary remains free to move. Within the Thiele framework, this reflects a breakdown of the rigid-particle approximation, as asymmetric constraints induce spin structure deformation and redistribute internal stresses through the lattice. These deformations are visible in Fig. 2b, right, as irregularities in the triangulated lattice, where the otherwise regular hexagonal arrangement of skyrmions is locally distorted. Such distortions appear as variations in effective bond lengths and angles between neighbouring skyrmions in the Delaunay triangulation, indicating areas of localized strain in the lattice. Figure 2c,d displays the average time-resolved displacement of each of the previously defined four classes of skyrmions, obtained by tracking the trajectories of colour-coded skyrmions throughout the duration of the bipolar pulse. Class M skyrmions exhibit substantial motion during the current pulse, whereas class I skyrmions show only minimal displacement. Strikingly, upon removal of the current drive, the absence of external forcing allows internal skyrmion–skyrmion interactions to restore equilibrium, yielding a recoil opposite to the prior current-driven motion, irrespective of the applied polarity. The low-current-driven dynamics occur within a deformable AFM skyrmion lattice and involve a transient local compression during the pulse, followed by interaction-mediated recoil after the current is switched off. In this regime, 'scattering' does not denote an isolated dilute two-body collision but rather a local recoil event of mobile skyrmions from pinned neighbours, embedded within the collective lattice response. This recoil reflects a relaxation process in which mobile skyrmions recoil from their pinned neighbours, with the restoring forces arising from skyrmion–skyrmion repulsion and the

https://doi.org/10.1038/s41567-026-03383-4

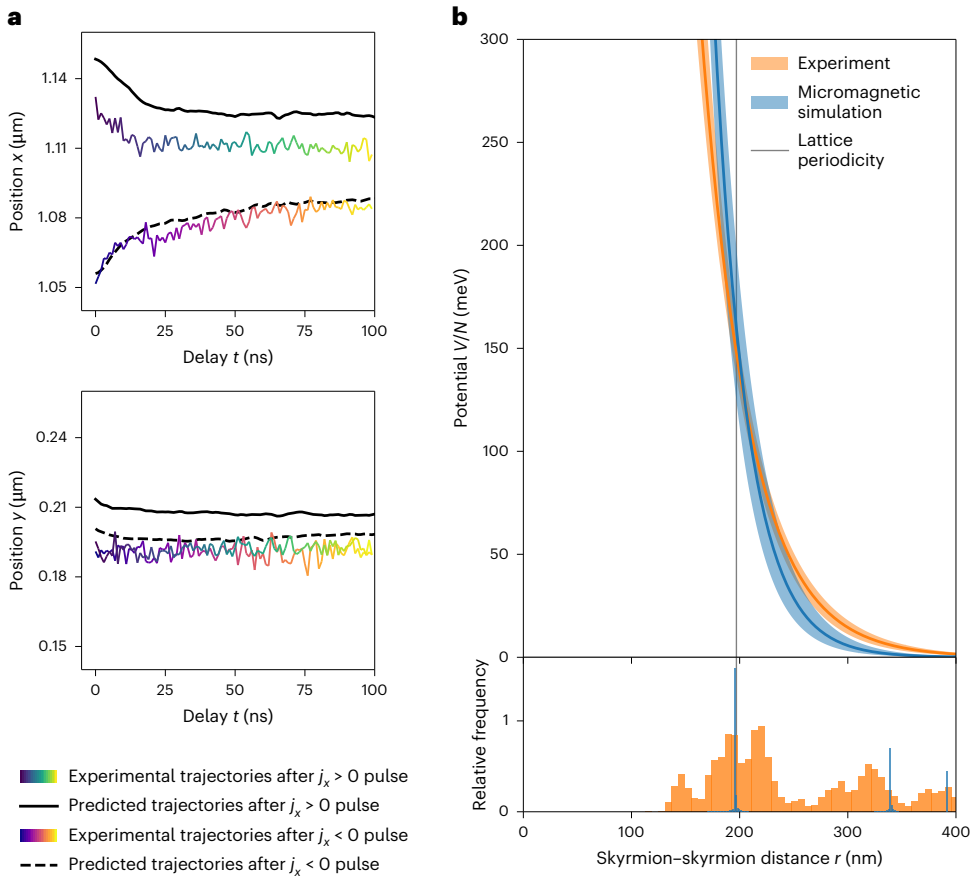


Fig. 3 | Quantitative extraction of the skyrmion–skyrmion interaction potential from the dynamics of skyrmions. a, Comparison between experimentally measured skyrmion trajectories and those predicted by the inverse method based on the Thiele equation for skyrmion R1, capturing their relaxation dynamics after the application of each polarity of the bipolar current pulse. Experimental trajectories are shown for both positive (blue to green) and negative (purple to yellow) current polarities, overlaid with model-predicted trajectories (dashed and solid black lines) obtained by numerical integration of the Thiele equation using the estimated interaction parameters a^* and b^*. **b**, The extracted skyrmion–skyrmion interaction potential per bilayer, $V_{(a^*,b^*)}(r)/N$, as a function of distance r, where N is the number of bilayer repetitions. Derived from the estimated force parameters, with experimental results (orange) compared with micromagnetic simulations (blue). Shaded regions indicate 68% uncertainty bands. Bottom: the skyrmion–skyrmion distances among skyrmions whose trajectories were predicted, as well as separations between those skyrmions and the boundary skyrmions, illustrating the range over which the potential is estimated by the data. The grey vertical line indicates the periodicity of the lattice.

surrounding pinning landscape. Rather than behaving as independent particles, the skyrmions respond collectively, revealing the elastically coupled and scattering-mediated nature of the lattice. This post-pulse relaxation is well described by an exponential decay, from which a characteristic relaxation time constant (τ_{relax}) is extracted for each skyrmion class. The recoil amplitudes and relaxation time constants vary substantially across the I, M, L and R classes, both in magnitude and decay rate, suggesting differences in the local energy landscape experienced by each group and thereby providing a quantitative measure of skyrmion interaction potential. A table with the extracted values of magnitude and decay rate for each of the four classes and both current polarities is given in Supplementary Section A1, Table 1. In the single-skyrmion limit, current-driven skyrmion dynamics are typically classified into pinned, creep and viscous-flow regimes[43,44], governed by the competition between driving forces, thermal excitations and the local energy landscape that governs pinning effects. With increasing skyrmion density, however, interactions become non-negligible[45] and qualitatively modify the dynamical response[46]. To explicitly distinguish these limits, we performed time-resolved measurements in the weakly interacting regime of spatially separated individual skyrmions (Supplementary Section A3), where the measurements show independent dynamics of each skyrmion governed by the local pinning landscape. By contrast, the dense lattice exhibits the additional incoherent-flow regime, in which the coexistence of pinned and mobile skyrmions gives rise to interaction-mediated correlated distortions and collective recoil. The viscous-flow regime is thus the dense-lattice analogue of the familiar high-drive flow regime of single skyrmions, whereas the incoherent-flow regime is a unique collective dynamic phase of the interacting lattice.

This complex behaviour now allows us to extract the skyrmion interaction potential directly from the nanosecond relaxation dynamics of L and R skyrmions, which lie at the lateral boundary between mobile and pinned regions. In this geometry, the pinned I skyrmions act as reference scattering centres, providing boundary conditions for quantifying the skyrmion–skyrmion interaction potential. We track the experimentally measured recoil trajectories of the L and R skyrmions following the termination of the nanosecond current pulse and employ an inverse estimation based on the Thiele equation (Methods; Supplementary Section B). In the fully compensated SyAFM configuration, the gyrotropic term contribution disappears, and long-range dipolar interactions are markedly suppressed, so that the dynamics reduce to a purely longitudinal balance between dissipative drag and the skyrmion–skyrmion force. By restricting the analysis to the immediate post-pulse relaxation window, we ensure that the motion is governed solely by skyrmion–skyrmion interactions and dissipation, free from external SOTs because the current is off and free

https://doi.org/10.1038/s41567-026-03383-4

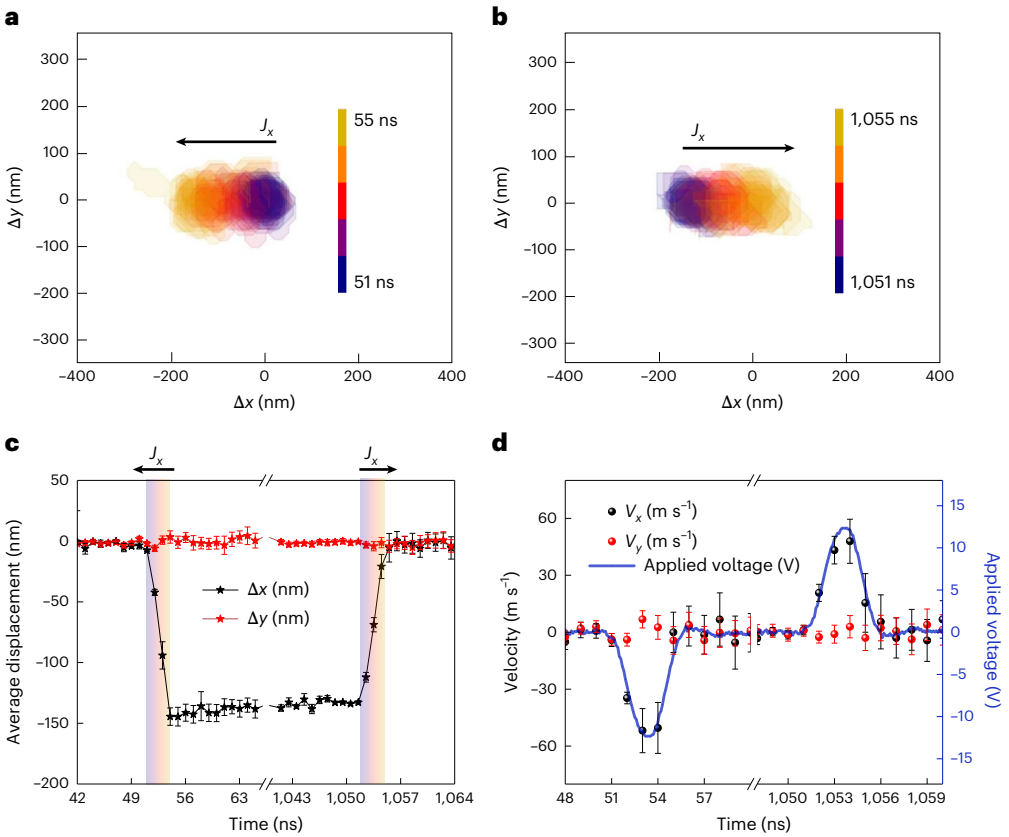


Fig. 4 | Nanosecond dynamics of AFM skyrmions in the coherent viscous-flow regime. a,**b**, Successive displacements of all individual skyrmions in sublattice A during the negative-current pulse (**a**) and positive-current pulse (**b**), respectively, for bipolar 2.5-ns current pulses of 1.2×10^{12} A m^{-2}, obtained by overlaying the contours of all 25 observed skyrmions at successive time steps, as indicated by the respective colour code. The displacements are given relative to the individual positions of skyrmions before applying the negative pulse at $t = 51$ ns and the positive pulse at $t = 1051$ ns for (**a**) and (**b**), respectively. The maintained coherence of the skyrmion overlay for all time steps indicates coherent motion of the whole skyrmion lattice. **c**, Average time-resolved displacement over 25 skyrmions along the x (black) and y (red) directions during the relevant time intervals. Shaded regions indicate the duration of negative or positive current pulses (J_x). **d**, Average time-resolved velocity components v_x (black) and v_y (red) of 25 skyrmions in response to the applied voltage (blue), illustrating a direct correlation between skyrmion motion and the external drive. The error bars in **c** and **d** denote the standard deviation of the skyrmion position and velocity, respectively, across the 25 skyrmion trajectories at each timepoint.

from stochastic thermal activation. $F(r)$ is the interaction force one skyrmion exerts on another along the line connecting their centres, arising from the energy cost of adapting the spin texture between them as the separation between their centres changes. In our SyAFM system, this force is mediated predominantly by short-range exchange and interfacial DMI, with only local interlayer magnetostatic contributions. This stands in sharp contrast to the behaviour of conventional FM skyrmions, whose interactions have been extensively characterized[25,28]. We model the repulsive interaction as a radially symmetric exponentially decaying force

$$\mathbf{F}_{(a,b)}(\mathbf{r}) = \frac{\mathbf{r}}{|\mathbf{r}|} F_{(a,b)}(|\mathbf{r}|), \quad \frac{F_{(a,b)}(r)}{D} = 1\,\mathrm{ms}^{-1} \exp\left(-\frac{r-b}{a}\right), \qquad (1)$$

where r is the skyrmion–skyrmion distance, a characterizes the steepness and effective range of the force and b determines the strength of the force, whereas D denotes the dissipation constant. In this geometry, the surrounding lattice enters through the instantaneous positions of all neighbouring skyrmions, such that the recoil dynamics are well described by an effective pairwise interaction kernel embedded in the many-body configuration. From the analysis of the scattering trajectories, we can determine only the ratio $F_{(a,b)}(r)/D$. As the prefactor 1 m s^{-1} is of the same order of magnitude as the velocities in the system, b is also of the same order of magnitude as the approximate effective interaction distance. This physically grounded parametrization provides direct experimental access to the microscopic interaction law in the regime where exchange and DMI become important, a regime that has so far remained experimentally elusive at the nanoscale.

Figure 3a shows, as an example for skyrmion R1, the experimental trajectory and the predicted trajectory obtained using the estimated interaction-potential parameters ($a^* = (44 \pm 4)$ nm, $b^* = (247 \pm 4)$ nm) (Methods and Supplementary Section B). Furthermore, micromagnetic simulations were carried out in a system closely matching the experimental dynamic simulation with skyrmion scattering, and the resulting interaction-potential parameters in this case are $a^* = (31 \pm 3)$ nm and $b^* = (288 \pm 13)$ nm (Supplementary Section B2). As the dissipation constant D in the experiment deviates from its value in a homogeneous, defect-free system due to nanoscale roughness[45,47,48], the force parameter b differs between the experiment and the value expected for a homogeneous, defect-free system. By comparing $F_{(a,b)}(r)$ over the relevant range of r in the experiment and in the homogeneous case, we infer that the effective dissipation constant D in the experiment is approximately four times larger than in a homogeneous system. By contrast, the parameter a does not depend on the value of D in the extraction of the potential. The interaction potential is then obtained via equation (1) with the respective D obtained via $V_{(a,b)}(r) = -\int \mathrm{d}r\, F_{(a,b)}(r)$, resulting in an exponentially decaying repulsive functional dependence. Figure 3b shows the experimentally estimated potential (orange) alongside the micromagnetic result (blue). Figure 3b, bottom, shows a histogram of skyrmion–skyrmion

https://doi.org/10.1038/s41567-026-03383-4

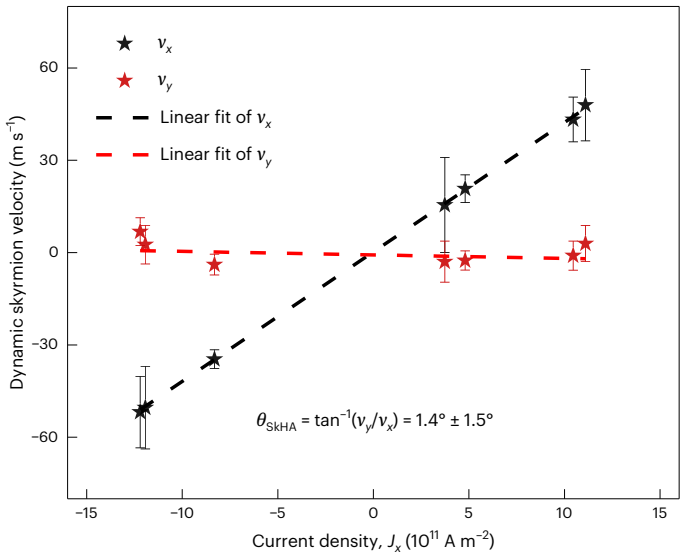


Fig. 5 | Suppression of the skyrmion Hall effect in the coherent viscous-flow regime. Dynamic skyrmion velocity components v_x (black stars) and v_y (red stars) as a function of applied current density J_x. Each data point represents the mean velocity obtained from 25 individually tracked skyrmion trajectories. The error bars denote the standard deviation across the 25 skyrmion trajectories at each current density. The skyrmion Hall angle θ_{SkHA} is obtained from the inverse tangent of the ratio of the slopes of the linear fits of v_y and v_x versus J_x, yielding 1.4° ± 1.5°, where the uncertainty denotes the standard error of the fitted slopes.

separations among skyrmions whose trajectories were predicted, as well as separations between those skyrmions and the boundary skyrmions, confirming that the potential is well constrained within the measurement window. The overlapping uncertainty bands between experiment and simulation validate the robustness of the inverse parameter estimation method and support the physical picture of a short-range, rapidly decaying repulsion governed by the finite spatial extent of the skyrmion spin texture. The overlap between experiment and simulation also shows that the dominant contributions in both cases were identified, and that the potential from the Thiele equation can be fully explained in this study from the underlying micromagnetism. Such a determination of potential is enabled by the unique L and R skyrmions that reside at the lateral boundary between mobile and immobile regions, experiencing a well-defined repulsive interaction with pinned I skyrmions that act as reference neighbours. This configuration produces reproducible skyrmion–skyrmion scattering trajectories that are absent in the conventional flow regime of skyrmion dynamics (discussed in the following section), where collective motion dominates and relative separations remain constant. This approach provides a direct and quantitative determination of the skyrmion–skyrmion interaction potential from the real-time relaxation of nanosecond scattering trajectories, without relying on equilibrium structure factors[25], thermal statistics[28] or other indirect inference methods. By extracting the potential from well-defined scattering events, we probe the interaction on its intrinsic length and timescales, accessing a regime previously unreachable in experiments. The potential has been tested against the dependence on skyrmion areal density and micromagnetic parameters (Supplementary Section B2). Although interaction potentials have been inferred in ferromagnetic systems, these measurements are largely qualitative[26,29], and quantitative estimates have relied on indirect approaches such as iterative Boltzmann inversion[28], which require thermal equilibrium and stochastic motion. Such conditions are inapplicable for dynamics that are reproducible over billions of cycles, which we, however, can analyse using our approach.

Coherent viscous-flow regime and the absence of both a skyrmion Hall effect and inertial effect

Next, we explore the high current density regime where all skyrmions move, allowing us to probe the viscous-flow regime. Previous static imaging before and after a current pulse injection has reported efficient and fast AFM skyrmion motion[19,21], based on position shifts measured before and after current pulses, without capturing the intermediate dynamics. However, ultrafast computation cannot be guaranteed by velocity alone, as inertial effects may set an upper bound on the response speed[49]. Although such measurements provide valuable insights into the net displacement, they leave open questions regarding the precise temporal evolution of skyrmion motion. In particular, the transient response, including inertial effects, is crucial for device applications, as the inertial lag and damping-controlled settling place a stringent upper bound on the clock frequency of skyrmion-based logic operations. Notably, substantial shape deformations and morphological changes have also been observed during motion[21], complicating the interpretation of underlying SOT-driven behaviour. In SyAFM systems, vertically coupled skyrmions in ferromagnetic layers exhibit opposite topological charges, leading to cancellation of the SkHE in the steady state. However, due to the finite interlayer exchange coupling strength, a transient separation between the skyrmions in the two-layer systems can arise during acceleration, giving rise to an effective inertial behaviour[50]. The magnitude and duration of this inertial response are strongly dependent on the strength of the interlayer exchange interaction, with weaker coupling leading to larger separations and longer relaxation times. Micromagnetic simulations predict that, upon the application of a current pulse, skyrmions in SyAFMs initially experience a partial transient separation due to the gyroforce before subsequently realigning due to strong AFM coupling[50].

To probe this dynamic response of the system, we perform time-resolved pump–probe X-ray microscopy under conditions where the applied current overcomes the local pinning potential for all skyrmions. The higher pulse voltage applied results in a four times higher current density of 1.2×10^{12} A m^{-2} and a shorter pulse duration of 2.5 ns was chosen to reduce the average heat load. We analyse the skyrmion trajectories within each sublattice and compare their motion relative to the current direction. In both sublattices, all skyrmions translate homogeneously along the direction of the applied current, as can be seen in Supplementary Video 3. To graphically visualize this motion, in Figs. 4a,b, the contours of all skyrmions are overlaid with their relative displacements during negative and positive pulses. This produces a real-space map of the motion for 25 skyrmions under the alternating current pulses, with the temporal progression encoded in the given colour scales. The resulting paths reveal that the skyrmions retrace symmetric trajectories under current reversal. The coherent overlap of contours defines the coherent viscous-flow regime, in which all skyrmions maintain fixed relative positions and move in phase as a rigid lattice, in contrast to the spatially uncorrelated motion observed in the incoherent regime. This collective motion is further quantified in Fig. 4c, where the average displacement over all skyrmions along the x-axis (black) reverses sign with current polarity, whereas the y-axis displacement (red) remains near zero throughout the bipolar cycle. This absence of a transverse drift indicates the suppression of the skyrmion Hall effect, a direct consequence of the opposing Magnus forces in the two sublattices in our SyAFM system. Remarkably, no delay or phase shift between the sublattices is detected within the 1-ns time resolution, indicating that our interlayer exchange coupling is sufficiently strong to suppress any measurable differential acceleration dynamics[50]. The corresponding velocity is extracted from the time-resolved displacement by evaluating the dynamic change in skyrmion position between consecutive images taken at a temporal spacing of 1 ns. The time evolution of the average dynamic skyrmion velocity components v_x and v_y is shown in Fig. 4d, together with the independently measured bipolar voltage pulse shape at the sample

position (blue). The velocity profile is symmetric and oscillatory, tracking the bipolar excitation without measurable delay, which indicates negligible inertia effects. The longitudinal component v_x (black points) dominates, remaining aligned with the current direction throughout the cycle, while the transverse component v_y (red points) only slightly fluctuates around zero. As the core polarity of skyrmions in both the sublattices is opposite, the forces arising from the topological charge term $\mathbf{G} \times \mathbf{v}$ act in opposite directions. When the skyrmions move together, these forces cancel each other, eliminating any net transverse deflection. This behaviour is a defining signature of the absence of the skyrmion Hall effect, indicating that the opposing Magnus forces within the AFM skyrmion lattice compensate each other, leading to suppression of transverse motion[18]. The dissipative forces, governed by the term $-\alpha D\mathbf{v}$, constructively add up, generating a net longitudinal velocity v_x, which can be expressed as $v_x = F_{ext}/2\alpha D$, where F_{ext} represents the external driving force. Here, D denotes the dissipative tensor of the AFM skyrmion. The external force driving the skyrmions is derived from the spin Hall effect and is expressed as $\mathbf{F}_{ext} = -\frac{\hbar}{4\pi e} J_x \theta_{SH} B$, where J_x is the applied current density, e is the charge of the electron, θ_{SH} is the spin Hall angle, and B represents a factor that defines the spin torque efficiency[40]. Note that no post-pulse relaxation or recoil is observed within the measurement resolution, indicating the absence of substantial pinning or scattering in this regime.

Figure 5 shows the current–density dependence of the dynamic skyrmion velocity components v_x and v_y, extracted from time-resolved measurements across a range of applied current densities. The longitudinal velocity v_x (black stars) shows a clear linear dependence on J_x, confirming that the skyrmion velocity scales proportionally with the applied drive, as expected in the viscous-flow regime where pinning is negligible[11]. The transverse velocity v_y (red stars) fluctuates around zero with no systematic trend, indicating that transverse deflection is entirely suppressed over the full range of current densities explored. The in-plane deflection of skyrmions is quantified by the skyrmion Hall angle, defined as $\theta_{SkHA} = \tan^{-1}(v_y/v_x)$. From the linear fits shown in Fig. 5, we extract a skyrmion Hall angle of 1.4° ± 1.5°, consistent with zero within experimental uncertainty. This result directly confirms the suppression of a measurable skyrmion Hall effect, independent of the magnitude or polarity of the applied current. This behaviour is in good agreement with theoretical predictions for compensated AFM skyrmion lattices, where the net topological charge vanishes, and the skyrmion Hall effect is fully suppressed[51]. Notably, the extracted skyrmion Hall angle remains zero within experimental uncertainty. In fully compensated systems, the SkHE vanishes when the effective angular momentum density, $\mathbf{L}_{eff}$, approaches zero. In ferrimagnets, the angular compensation point may differ from the magnetization compensation point due to unequal sublattice gyromagnetic ratios γ, especially in rare-earth/transition-metal alloys. By contrast, our SyAFM stack, composed of CoFeB and CoB with nearly identical γ, is designed to align both compensation points, theoretically eliminating the SkHE. The small residual deflection observed may result from slight asymmetries in γ or interfacial properties.

Conclusion

By exploiting skyrmion dynamics from the pinned to the viscous-flow regime across the previously unexplored incoherent dynamics regime, we explore skyrmion motion and scattering. Our results reveal the full spatiotemporal dynamics of an AFM skyrmion lattice in a synthetic antiferromagnet, exposing the key mechanisms that govern its collective behaviour. By tuning the excitation amplitude, we access two distinct dynamical regimes: a fragmented, incoherent flow at low-current densities and a coherent, rigid-lattice translation at higher drives. In the lower-drive range, the pinned skyrmions act as scattering centres for the mobile ones, and after the latter have been driven toward them by SOTs, once the current pulse terminates, the resulting repulsive interaction produces a recoil motion, with a characteristic timescale of 3–20 ns, that is, opposite to the drive direction. This scattering-mediated recoil allows us to sample the underlying skyrmion–skyrmion interaction potential, enabling its quantitative extraction from the measured relaxation dynamics. We find excellent agreement with micromagnetic simulations, matching both the magnitude and range of the repulsive interaction. Upon increasing the excitation, the system undergoes a transition into a viscous-flow regime. The high temporal resolution of our measurements enables direct tracking of real-space AFM skyrmion trajectories, revealing purely longitudinal motion across a wide range of current densities. Importantly, the dynamics are highly reproducible, with virtually no observable inertia, no transverse drift and no discernible deformation, underscoring the inherent robustness of AFM skyrmion dynamics. Ultrafast operation demands not only fast velocity but also negligible inertia. Our findings directly show that AFM skyrmion dynamics fulfil these criteria, enabling robust gigahertz-class operation in ultra-dense information and logic devices. The stability of the skyrmion lattice even at high current densities suggests that AFM skyrmions can overcome key limitations of their ferromagnetic counterparts, particularly in terms of robustness against pinning and stochastic motion. Optimizing interlayer coupling, DMI and interfacial magnetic anisotropies could lead to further enhanced control over AFM skyrmion dynamics. Our work establishes a quantitative foundation for future exploration of AFM topological textures and paves the way for low-power, robust and scalable spintronic devices built on AFM skyrmions.

Online content

Any methods, additional references, Nature Portfolio reporting summaries, source data, extended data, supplementary information, acknowledgements, peer review information; details of author contributions and competing interests; and statements of data and code availability are available at https://doi.org/10.1038/s41567-026-03383-4.

References

1. Wolf, S. A. et al. Spintronics: a spin-based electronics vision for the future. *Science* **294**, 1488–1495 (2001).
2. Parkin, S. S., Hayashi, M. & Thomas, L. Magnetic domain-wall racetrack memory. *Science* **320**, 190–194 (2008).
3. Bogdanov, A. N. & Yablonskii, D. Thermodynamically stable 'vortices' in magnetically ordered crystals. The mixed state of magnets. *Zh. Eksp. Teor. Fiz.* **95**, 178 (1989).
4. Mühlbauer, S. et al. Skyrmion lattice in a chiral magnet. *Science* **323**, 915–919 (2009).
5. Fert, A., Cros, V. & Sampaio, J. Skyrmions on the track. *Nat. Nanotechnol.* **8**, 152–156 (2013).
6. Everschor-Sitte, K., Masell, J., Reeve, R. M. & Kläui, M. Perspective: magnetic skyrmions-overview of recent progress in an active research field. *J. Appl. Phys.* **124**, 240901 (2018).
7. Nagaosa, N. & Tokura, Y. Topological properties and dynamics of magnetic skyrmions. *Nat. Nanotechnol.* **8**, 899–911 (2013).
8. Büttner, F., Lemesh, I. & Beach, G. S. Theory of isolated magnetic skyrmions: from fundamentals to room temperature applications. *Sci. Rep.* **8**, 4464 (2018).
9. Woo, S. et al. Observation of room-temperature magnetic skyrmions and their current-driven dynamics in ultrathin metallic ferromagnets. *Nat. Mater.* **15**, 501–506 (2016).
10. Jiang, W. et al. Direct observation of the skyrmion Hall effect. *Nat. Phys.* **13**, 162–169 (2017).
11. Litzius, K. et al. Skyrmion Hall effect revealed by direct time-resolved x-ray microscopy. *Nat. Phys.* **13**, 170–175 (2017).
12. Luo, S. et al. Reconfigurable skyrmion logic gates. *Nano Lett.* **18**, 1180–1184 (2018).
13. Tomasello, R. et al. A strategy for the design of skyrmion racetrack memories. *Sci. Rep.* **4**, 6784 (2014).

14. Zhang, X., Ezawa, M. & Zhou, Y. Magnetic skyrmion logic gates: conversion, duplication and merging of skyrmions. *Sci. Rep.* **5**, 9400 (2015).
15. Song, K. M. et al. Skyrmion-based artificial synapses for neuromorphic computing. *Nat. Electron.* **3**, 148–155 (2020).
16. Da Câmara Santa Clara Gomes, T. et al. Neuromorphic weighted sums with magnetic skyrmions. *Nat. Electron.* **8**, 204–214 (2025).
17. Zhang, X., Zhou, Y. & Ezawa, M. Antiferromagnetic skyrmion: stability, creation and manipulation. *Sci. Rep.* **6**, 24795 (2016).
18. Barker, J. & Tretiakov, O. A. Static and dynamical properties of antiferromagnetic skyrmions in the presence of applied current and temperature. *Phys. Rev. Lett.* **116**, 147203 (2016).
19. Dohi, T., DuttaGupta, S., Fukami, S. & Ohno, H. Formation and current-induced motion of synthetic antiferromagnetic skyrmion bubbles. *Nat. Commun.* **10**, 5153 (2019).
20. Dohi, T. et al. Enhanced thermally-activated skyrmion diffusion in synthetic antiferromagnetic systems with tunable effective topological charge. *Nat. Commun.* **14**, 5424 (2023).
21. Pham, V. T. et al. Fast current-induced skyrmion motion in synthetic antiferromagnets. *Science* **384**, 307–312 (2024).
22. Legrand, W. et al. Room-temperature stabilization of antiferromagnetic skyrmions in synthetic antiferromagnets. *Nat. Mater.* **19**, 34–42 (2020).
23. Winkler, T. B. et al. Coarse-graining collective skyrmion dynamics in confined geometries. *Appl. Phys. Lett.* **124**, 022403 (2024).
24. Zhang, X. et al. Skyrmion–skyrmion and skyrmion-edge repulsions in skyrmion-based racetrack memory. *Sci. Rep.* **5**, 7643 (2015).
25. Huang, P. et al. Melting of a skyrmion lattice to a skyrmion liquid via a hexatic phase. *Nat. Nanotechnol.* **15**, 761–767 (2020).
26. Du, H. et al. Interaction of individual skyrmions in a nanostructured cubic chiral magnet. *Phys. Rev. Lett.* **120**, 197203 (2018).
27. Rózsa, L. et al. Skyrmions with attractive interactions in an ultrathin magnetic film. *Phys. Rev. Lett.* **117**, 157205 (2016).
28. Ge, Y. et al. Constructing coarse-grained skyrmion potentials from experimental data with iterative Boltzmann inversion. *Commun. Phys.* **6**, 30 (2023).
29. Shimojima, T. et al. Nano-to-micro spatiotemporal imaging of magnetic skyrmion's life cycle. *Sci. Adv.* **7**, eabg1322 (2021).
30. Woo, S. et al. Deterministic creation and deletion of a single magnetic skyrmion observed by direct time-resolved x-ray microscopy. *Nat. Electron.* **1**, 288–296 (2018).
31. Kern, L.-M. et al. Emergent chaos-like dynamics of spin–orbit-torque-driven magnetic transitions. *Small* **22**, e73778 (2026).
32. Gao, S. et al. Fractional antiferromagnetic skyrmion lattice induced by anisotropic couplings. *Nature* **586**, 37–41 (2020).
33. Akosa, C. A., Tretiakov, O., Tatara, G. & Manchon, A. Theory of the topological spin hall effect in antiferromagnetic skyrmions: impact on current-induced motion. *Phys. Rev. Lett.* **121**, 097204 (2018).
34. Göbel, B., Schimpf, L. & Mertig, I. Topological orbital hall effect caused by skyrmions and antiferromagnetic skyrmions. *Commun. Phys.* **8**, 17 (2025).
35. Thiele, A. A. Steady-state motion of magnetic domains. *Phys. Rev. Lett.* **30**, 230–233 (1973).
36. Msiska, R., Rodrigues, D. R., Leliaert, J. & Everschor-Sitte, K. Nonzero skyrmion hall effect in topologically trivial structures. *Phys. Rev. Appl.* **17**, 064015 (2022).
37. Dzyaloshinsky, I. A thermodynamic theory of 'weak' ferromagnetism of antiferromagnetics. *J. Phys. Chem. Solids* **4**, 241–255 (1958).
38. Moriya, T. Anisotropic superexchange interaction and weak ferromagnetism. *Phys. Rev.* **120**, 91 (1960).
39. Bhukta, M. et al. Homochiral antiferromagnetic merons, antimerons and bimerons realized in synthetic antiferromagnets. *Nat. Commun.* **15**, 1641 (2024).
40. Dohi, T. et al. Observation of a non-reciprocal skyrmion hall effect of hybrid chiral skyrmion tubes in synthetic antiferromagnetic multilayers. *Nat. Commun.* **16**, 8285 (2025).
41. Lemesh, I. et al. Current-induced skyrmion generation through morphological thermal transitions in chiral ferromagnetic heterostructures. *Adv. Mater.* **30**, 1805461 (2018).
42. Zázvorka, J. et al. Skyrmion lattice phases in thin film multilayer. *Adv. Funct. Mater.* **30**, 2004037 (2020).
43. Song, D. et al. Steady motion of 80-nm-size skyrmions in a 100-nm-wide track. *Nat. Commun.* **15**, 5614 (2024).
44. Peng, L. et al. Dynamic transition of current-driven single-skyrmion motion in a room-temperature chiral-lattice magnet. *Nat. Commun.* **12**, 6797 (2021).
45. Reichhardt, C., Reichhardt, C. J. O. & Milošević, M. Statics and dynamics of skyrmions interacting with disorder and nanostructures. *Rev. Mod. Phys.* **94**, 035005 (2022).
46. Reichhardt, C., McDermott, D. & Reichhardt, C. Characterizing skyrmion flow phases with principal component analysis. *Phys. Rev. Res.* **8**, 013045 (2026).
47. Zázvorka, J. et al. Thermal skyrmion diffusion used in a reshuffler device. *Nat. Nanotechnol.* **14**, 658–661 (2019).
48. Brems, M. A. et al. Realizing quantitative quasiparticle modeling of skyrmion dynamics in arbitrary potentials. *Phys. Rev. Lett.* **134**, 046701 (2025).
49. Büttner, F. et al. Dynamics and inertia of skyrmionic spin structures. *Nat. Phys.* **11**, 225–228 (2015).
50. Panigrahy, S., Mallick, S., Sampaio, J. & Rohart, S. Skyrmion inertia in synthetic antiferromagnets. *Phys. Rev. B* **106**, 144405 (2022).
51. Zhang, X., Zhou, Y. & Ezawa, M. Magnetic bilayer-skyrmions without skyrmion Hall effect. *Nat. Commun.* **7**, 10293 (2016).

Publisher's note Springer Nature remains neutral with regard to jurisdictional claims in published maps and institutional affiliations.

Open Access This article is licensed under a Creative Commons Attribution 4.0 International License, which permits use, sharing, adaptation, distribution and reproduction in any medium or format, as long as you give appropriate credit to the original author(s) and the source, provide a link to the Creative Commons licence, and indicate if changes were made. The images or other third party material in this article are included in the article's Creative Commons licence, unless indicated otherwise in a credit line to the material. If material is not included in the article's Creative Commons licence and your intended use is not permitted by statutory regulation or exceeds the permitted use, you will need to obtain permission directly from the copyright holder. To view a copy of this licence, visit http://creativecommons.org/licenses/by/4.0/.

© The Author(s) 2026

Methods

Material deposition

The thin-film material stacks investigated in this study were deposited using a Singulus Rotaris magnetron-sputtering system at a base pressure of 4×10^{-8} mbar and room temperature. All layers were deposited by direct current-magnetron sputtering using pure argon as sputtering gas. To minimize pinning effects, low deposition power and low argon flow rate were carefully selected as process parameters. The resulting smoothness of the individual layers was verified using X-ray reflectivity measurements. The SyAFM multilayer consists of $Co_{0.8}B_{0.2}$ (CB, 1.1 nm) as sublattice B and a bilayer combination of $Co_{0.6}Fe_{0.2}B_{0.2}$ (CFB, 0.2 nm) and $Fe_{0.6}Co_{0.2}B_{0.2}$ (FCB, 0.4 nm) as sublattice A. This compositional asymmetry enables element-selective X-ray magnetic circular dichroism (XMCD) imaging: the Fe L_3 edge selectively probes sublattice A, whereas the Co L_3 contrast predominantly probes sublattice B. Although the two sublattices differ in both thickness and material composition, the stack is designed such that $M_{s,A}\, t_A \approx M_{s,B}\, t_B$, as seen in the Supplementary Fig. S1. Here, t_A and t_B denote the thicknesses of ferromagnetic sublattices A and B, respectively, and $M_{s,A}$ and $M_{s,B}$ their corresponding saturation magnetizations. The effective saturation magnetization is defined as $M_s^{\mathrm{eff}} = \frac{M_{s,A}t_A + M_{s,B}t_B}{t_A + t_B}$, and the SQUID magnetometer yields $M_s^{\mathrm{eff}} = (0.85 \pm 0.15) \times 10^6\ \mathrm{A\,m^{-1}}$. The interlayer exchange coupling strength is estimated from the saturation field extracted from the in-plane (hard-axis) hysteresis loops, yielding $J_{\mathrm{IEC}} \approx (0.38 \pm 0.07)\ \mathrm{mJ\,m^{-2}}$. Cross-sectional high-angle annular dark-field scanning transmission electron microscopy and energy-dispersive X-ray spectroscopy measurements of the SyAFM stack confirm a continuous multilayer without structural discontinuities or large-scale compositional inhomogeneities (Supplementary Section A2). The observed columnar grain structure and nanoscale interface roughness introduce local variations in effective magnetic parameters (for example, K_{eff}, DMI and interlayer exchange), which generate a spatially inhomogeneous energy landscape and can act as the dominant pinning mechanism.

Microfabrication

The SyAFM is deposited onto a silicon nitride membrane window together with 200-nm-thick Au contact pads at both ends that enable the application of electrical current pulses along the strips. The track structures were defined using electron beam lithography on a bilayer resist, followed by lift-off processing. A second lithography step was employed to pattern the contact pads, after which the Cr(5 nm)/Au(200 nm) bilayer was deposited via sputtering under a base pressure of 5×10^{-7} mbar. To minimize heat accumulation in the 100-nm-thick silicon nitride membrane, whose low thickness limits heat dissipation, we introduce a 1-µs delay between successive alternating current pulses, ensuring stable measurement conditions over billions of pump–probe cycles.

Time-resolved STXM imaging

The XMCD imaging experiments were performed at the MAXYMUS end station[52] of the BESSY II synchrotron, operated by the Helmholtz–Zentrum Berlin. XMCD imaging exploits the differential absorption of left- and right-circularly polarized X-rays, which depends on the magnetization direction within a material. This technique provides element-specific contrast by tuning the incident X-ray energy to the absorption edges of transition metals, allowing direct imaging of the local magnetic configuration. In this study, time-resolved STXM was employed to capture the real-space magnetization profile. Moreover, the X-ray absorption spectra were recorded before imaging, confirming the resonance conditions for Fe and Co at photon energies of approximately 708.1 eV and 778.6 eV, respectively. The unambiguous contrast inversion between sublattices verified the strong AFM coupling, as observed in static and dynamic imaging sequences. The stability of this coupling was further confirmed by maintaining the characteristic XMCD contrast throughout the entire range of applied current densities. This methodology, enabled by high-brightness synchrotron radiation, provides a powerful platform for investigating current-driven magnetization dynamics with both 20-nm spatial and subnanosecond temporal resolution. Time-resolved pump–probe measurements were performed to capture the nanosecond-scale dynamics of the skyrmion lattice. The experiment utilized a 2001-channel time-resolved detection scheme, enabling precise reconstruction of skyrmion motion over the entire excitation cycle. A bipolar current pulse sequence was applied, with a 1-µs delay between successive positive and negative pulses, ensuring reproducible skyrmion trajectories without cumulative heating effects. Various bipolar current-pulse widths of 2.5, 5, 7.5 and 10 ns were used in the different measurements; the pulse sequence shown in Fig. 1e corresponds to a pulse width of 5 ns. Although all measurements were conducted at room temperature, a residual helium gas pressure of 10 mbar was maintained in the system to enable additional thermal dissipation and mitigate temperature-induced artifacts.

For the dynamic analysis, the skyrmion position was determined at each pump–probe delay time from the time-resolved XMCD–STXM images. By scanning the delay in steps of 1 ns, we reconstructed the skyrmion trajectory throughout the excitation cycle. The dynamic skyrmion velocity was then obtained from the temporal derivative of the displacement, that is, from the change in skyrmion position between consecutive delay frames divided by the corresponding time interval. Thus, unlike conventional approaches that rely on static images taken before and after the pulse that infer a net velocity from the total displacement after pulse injection, our method yields a time-resolved dynamic velocity during and after the current pulse. Possible effects of Joule heating during current excitation are discussed in Supplementary Section A4.

Classification of skyrmions based on their trajectories

Skyrmions are classified based on their time-resolved trajectories obtained from pump–probe measurements. The classification is defined by their distinct dynamical responses during the bipolar current pulse cycle. Specifically, three qualitatively distinct dynamical behaviours are observed. Immobile skyrmions (class I) exhibit minimal motion during the current pulse, followed by pronounced recoil after its termination, and their dynamics are the same for both current pulse polarities. Mobile skyrmions (class M), which are only weakly affected by pinning, translate smoothly during the pulse and show minimal post-pulse relaxation. Their dynamics are also symmetric for both current polarities (they move at the same speed just in opposite directions, and the traces shown in Supplementary Fig. 4a overlap for both current polarities). In addition, a third type of trajectory is observed for skyrmions located at the boundary of the pinned region. These skyrmions exhibit intermediate displacement but, importantly, show strongly asymmetric deformation and recoil dynamics with respect to current polarity. Their dynamics are not the same for both polarities (visible as their traces for both current polarities shown in Supplementary Fig. 4b do not overlap). They are classified as L and R according to their spatial position relative to the class I skyrmions (left or right boundary). In the dataset shown in Fig. 2, approximately 66% of skyrmions belong to the mobile class (M), 18% are immobile (class I) and the remaining 16% (L/R) are located at the boundaries of the immobile regions, exhibiting distinct boundary dynamics.

We note that while the displacement amplitudes remain comparable for $+J_x$ and $-J_x$ across all skyrmion classes, as shown in Table 1 of Supplementary Section A1, the corresponding relaxation times exhibit a polarity-dependent variation, particularly pronounced for the asymmetrically positioned L and R boundary skyrmions. The displacement amplitude is primarily set by the magnitude of the SOT-driven local compression and distortion induced during the pulse, which is equal in magnitude for both polarities. By contrast, the relaxation time τ_{relax} is governed by the local energy landscape sampled during post-pulse

recoil, arising from the combined effects of pinning and skyrmion–skyrmion interactions. As opposite current polarities displace skyrmions in opposite directions, the subsequent recoil traverses spatially distinct regions of this heterogeneous landscape, naturally leading to different relaxation timescales for $+J_x$ and $-J_x$.

Determination of the skyrmion–skyrmion interaction potential from scattering trajectories

To determine the optimum values for the parameters (a^*,b^*) in the definition of the skyrmion interaction potential, that lead to the best agreement with the observed recoil trajectories, we consider the range of interaction potentials parametrized by a and b within a reasonable interval, for which we numerically integrate the Thiele equation and obtain the corresponding trajectories for the L and R classes of skyrmions (Supplementary Section B). The optimal interaction parameters (a^*,b^*) and their uncertainties are extracted from the loss landscape $L_2(a,b)$ (Supplementary Section B). This approach constitutes a direct determination of the interaction potential from the real-time relaxation of nanosecond scattering trajectories, without relying on indirect methods of determination. The best-fit parameters are $a^* = (44 \pm 4)$ nm and $b^* = (247 \pm 4)$ nm for the experiment. The experimentally measured positions of the surrounding pinned I skyrmions are incorporated in the Thiele equation as dynamic boundary conditions, ensuring that the influence of the local skyrmion environment is accurately included. The starting positions for the predicted trajectories are determined from the experimental data. These predicted trajectories are directly compared with the experimentally observed trajectories via the loss function $L_2(a,b)$, defined as a measure for the deviation between prediction and experiment over the early-time relaxation window.

Data availability

The data supporting the findings of this study are available within the Article and its Supplementary Information. Source data are provided with this paper. These data are also available via Zenodo at https://doi.org/10.5281/zenodo.20640670 (ref. 53).

Code availability

All simulations were performed using established commercial or publicly available software. All source codes are available from the corresponding authors upon reasonable request.

References

52. Follath, R., Schmidt, J., Weigand, M. & Fauth, K. The X-ray microscopy beamline UE46-PGM2 at BESSY. *AIP Conf. Proc.* **1234**, 323–326 (2010).
53. Bhukta, M. et al. Source data—Time-resolved imaging of antiferromagnetic skyrmion interactions. *Zenodo* https://doi.org/10.5281/zenodo.20640670 (2026).

Acknowledgements

We thank the Helmholtz–Zentrum Berlin für Materialien und Energie GmbH for the allocation of synchrotron radiation beamtime at the Maxymus end station. We acknowledge the Paul Scherrer Institut, Villigen, Switzerland, for the allocation of synchrotron radiation beamtime at the PolLux end station of the Swiss Light Source (SLS). M.K. acknowledges the hospitality of the Lawrence Berkeley National Laboratory.

Author contributions

T. Dohi, R.F. and M.K. conceived and supervised the project. T. Dohi and M.A.S. deposited the multilayer stack. M.B. precharacterized the samples by SQUID magnetometer and MFM imaging, fabricated the devices by electron-beam lithography, fabricated the electrical contacts and carried out the Joule-heating measurements. M.B. carried out and supervised the STXM experiments and analysed the data with support from S.W., M.W., S.F., J.R. and H.O. M.B., T. Dohi, F.K. and D.M.T. participated in the time-resolved STXM beamtime experiments. T. Denneulin, J.V.V. and R.E.D.-B. conducted and analysed the high-angle annular dark-field scanning transmission electron microscopy and energy-dispersive X-ray spectroscopy measurements. K.L. conceived and established the trajectory-based interaction-potential analysis and performed the micromagnetic simulations. All authors participated in the discussion and interpreted the results. M.B. drafted the manuscript with input from K.L., T. Dohi, R.F. and M.K. All authors discussed the results and commented on the manuscript.

Funding

Open access funding provided by Johannes Gutenberg-Universität Mainz. The PolLux end station was financed by the German Ministerium für Bildung und Forschung (BMBF) through ErUM-Pro contract nos. 05K16WED, 05K19WE2 and 05K22WE2. This research used resources of the Advanced Light Source, which is a DOE Office of Science User Facility under contract no. DE-AC02-05CH1123. This work has received funding from the European Union's Horizon 2020 research and innovation programme under the Marie Skłodowska-Curie Grant agreement no. 860060 'Magnetism and the effect of Electric Field' (MagnEFi), as well as from ERC Synergy grant no. 856538, project '3D-MAGiC,' the Horizon Europe project no. 101070290 (NIMFEIA), and Horizon Europe Programme Horizon 1.2 under the Marie Skłodowska-Curie Actions (MSCA), grant agreement no. 101119608 (TOPOCOM). It has also been supported by the Deutsche Forschungsgemeinschaft (DFG, German Research Foundation)—SPP 2137 Skyrmionics (project no. 462597720), TRR 173–268565370 (projects A01, A12 and B02) and the Dynamics and Topology Center TopDyn funded by the State of Rhineland Palatinate. This work was also partly supported by the Norwegian Research Council through its Center of Excellence, project no. 262633, 'QuSpin'. This work was partly supported by JSPS Kakenhi (grant nos. 23K13655, 24H00039, 24H00409 and 25K01645) as well as the Center for Science and Innovation in Spintronics at Tohoku University (Cooperative Research Project). This work was partly supported by the National Research Council of Science and Technology (NST) grant by the Korean government, MSIT (grant no. GTL24041-000).

Competing interests

The authors declare no conflicts of interest.

Additional information

Supplementary information The online version contains supplementary material available at https://doi.org/10.1038/s41567-026-03383-4.

Correspondence and requests for materials should be addressed to Takaaki Dohi, Robert Frömter or Mathias Kläui.

Peer review information *Nature Physics* thanks Haifeng Du and the other, anonymous, reviewer(s) for their contribution to the peer review of this work. Peer reviewer reports are available.

Reprints and permissions information is available at www.nature.com/reprints.